HHS Public Access

Author manuscript

IEEE Trans Med Imaging. Author manuscript; available in PMC 2017 June 08.

Published in final edited form as:

IEEE Trans Med Imaging. 2017 May ; 36(5): 1116–1128. doi:10.1109/TMI.2017.2650960.

Low-rank and Adaptive Sparse Signal (LASSI) Models for Highly Accelerated Dynamic Imaging

Saiprasad Ravishankar [Member, IEEE], **Brian E. Moore [Student Member, IEEE]**, **Raj Rao Nadakuditi [Member, IEEE]**, and **Jeffrey A. Fessler [Fellow, IEEE]**

Department of Electrical Engineering and Computer Science, University of Michigan, Ann Arbor, MI, 48109 USA

Abstract

Sparsity-based approaches have been popular in many applications in image processing and imaging. Compressed sensing exploits the sparsity of images in a transform domain or dictionary to improve image recovery from undersampled measurements. In the context of inverse problems in dynamic imaging, recent research has demonstrated the promise of sparsity and low-rank techniques. For example, the patches of the underlying data are modeled as sparse in an adaptive dictionary domain, and the resulting image and dictionary estimation from undersampled measurements is called dictionary-blind compressed sensing, or the dynamic image sequence is modeled as a sum of low-rank and sparse (in some transform domain) components (L+S model) that are estimated from limited measurements. In this work, we investigate a data-adaptive extension of the L+S model, dubbed LASSI, where the temporal image sequence is decomposed into a low-rank component and a component whose spatiotemporal (3D) patches are sparse in some adaptive dictionary domain. We investigate various formulations and efficient methods for jointly estimating the underlying dynamic signal components and the spatiotemporal dictionary from limited measurements. We also obtain efficient sparsity penalized dictionary-blind compressed sensing methods as special cases of our LASSI approaches. Our numerical experiments demonstrate the promising performance of LASSI schemes for dynamic magnetic resonance image reconstruction from limited k-t space data compared to recent methods such as k-t SLR and L+S, and compared to the proposed dictionary-blind compressed sensing method.

Index Terms

Dynamic imaging; Structured models; Sparse representations; Dictionary learning; Inverse problems; Magnetic resonanace imaging; Machine learning; Nonconvex optimization

I. Introduction

Sparsity-based techniques are popular in many applications in image processing and imaging. Sparsity in either a fixed or data-adaptive dictionary or transform is fundamental to the success of popular techniques such as compressed sensing that aim to reconstruct images from limited sensor measurements. In this work, we focus on low-rank and adaptive

S. Ravishankar and B. E. Moore are equal contributors.

dictionary-sparse models for dynamic imaging data and exploit such models to perform image reconstruction from limited (compressive) measurements. In the following, we briefly review compressed sensing (CS), CS-based magnetic resonance imaging (MRI), and dynamic data modeling, before outlining the contributions of this work.

A. Background

CS [1]–[4] is a popular technique that enables recovery of signals or images from far fewer measurements (or at a lower rate) than the number of unknowns or than required by Nyquist sampling conditions. CS assumes that the underlying signal is sparse in some transform domain or dictionary and that the measurement acquisition procedure is incoherent in an appropriate sense with the dictionary. CS has been shown to be very useful for MRI [5], [6]. MRI is a relatively slow modality because the data, which are samples in the Fourier space (or k-space) of the object, are acquired sequentially in time. In spite of advances in scanner hardware and pulse sequences, the rate at which MR data are acquired is limited by MR physics and physiological constraints [5].

CS has been applied to a variety of MR techniques such as static MRI [5], [7], [8], dynamic MRI (dMRI) [6], [9]–[11], parallel imaging (pMRI) [12]–[15], and perfusion imaging and diffusion tensor imaging (DTI) [16]. For static MR imaging, CS-based MRI (CSMRI) involves undersampling the k-space data (e.g., collecting fewer phase encodes) using random sampling techniques to accelerate data acquisition. However, in dynamic MRI the data is inherently undersampled because the object is changing as the data is being collected, so in a sense *all* dynamic MRI scans (of k-t space) involve some form of CS because one must reconstruct the dynamic images from under-sampled data. The traditional approach to this problem in MRI is to use “data sharing” where data is pooled in time to make sets of k-space data (e.g., in the form of a Casorati matrix [17]) that appear to have sufficient samples, but these methods do not fully model the temporal changes in the object. CS-based dMRI can achieve improved temporal (or spatial) resolution by using more explicit signal models rather than only implicit k-space data sharing, albeit at the price of increased computation.

CSMRI reconstructions with fixed, non-adaptive signal models (e.g., wavelets or total variation sparsity) typically suffer from artifacts at high undersampling factors [18]. Thus, there has been growing interest in image reconstruction methods where the dictionary is adapted to provide highly sparse representations of data. Recent research has shown benefits for such data-driven adaptation of dictionaries [19]–[22] in many applications [18], [23]–[25]. For example, the DLMRI method [18] jointly estimates the image and a synthesis dictionary for the image patches from undersampled k-space measurements. The model there is that the unknown (vectorized) image patches can be well approximated by a sparse linear combination of the columns or atoms of a learned (a priori unknown) dictionary D. This idea of joint dictionary learning and signal reconstruction from undersampled measurements [18], known as (dictionary) blind compressed sensing (BCS) [26], has been the focus of several recent works (including for dMRI reconstruction) [18], [27]–[36]. The BCS problem is harder than conventional (non-adaptive) compressed sensing. However, the dictionaries learned in BCS typically reflect the underlying image properties better than pre-determined models, thus improving image reconstructions.

While CS methods use sparse signal models, various alternative models have been explored for dynamic data in recent years. Several works have demonstrated the efficacy of low-rank models (e.g., by constraining the Casorati data matrix to have low-rank) for dynamic MRI reconstruction [17], [37]– [39]. A recent work [40] also considered a low-rank property for local space-time image patches. For data such as videos (or collections of related images [41]), there has been growing interest in decomposing the data into the sum of a low-rank (L) and a sparse (S) component [42]–[44]. In this L+S (or equivalently Robust Principal Component Analysis (RPCA) [42]) model, the L component may capture the background of the video, while the S component captures the sparse (dynamic) foreground. The L+S model has been recently shown to be promising for CS-based dynamic MRI [45], [46]. The S component of the L+S decomposition could either be sparse by itself or sparse in some known dictionary or transform domain. Some works alternatively consider modeling the dynamic image sequence as both low-rank and sparse (L & S) [47], [48], with a recent work [49] learning dictionaries for the S part of L & S. In practice, which model provides better image reconstructions may depend on the specific properties of the underlying data.

When employing the L+S model, the CS reconstruction problem can be formulated as follows:

$$\min_{x_L, x_S} \frac{1}{2}\|A(x_L + x_S) - d\|_2^2 + \lambda_L \|R_1(x_L)\|_* + \lambda_S \|T x_S\|_1. \quad \text{(P0)}$$

In (P0), the underlying unknown dynamic object is $x = x_L + x_S \in \mathbb{C}^{N_x N_y N_t}$, where x_L and x_S are vectorized versions of space-time (3D) tensors corresponding to N_t temporal frames, each an image[1] of size $N_x \times N_y$. The operator A is the sensing or encoding operator and d denotes the (undersampled) measurements. For parallel imaging with N_c receiver coils, applying the operator A involves frame-by-frame multiplication by coil sensitivities followed by applying an undersampled Fourier encoding (i.e., the SENSE method) [50]. The operation $R_1(x_L)$ reshapes x_L into an $N_x N_y \times N_t$ matrix, and $\|\cdot\|_*$ denotes the nuclear norm that sums the singular values of a matrix. The nuclear norm serves as a convex surrogate for matrix rank in (P0). Traditionally, the operator T in (P0) is a *known* sparsifying transform for x_S, and λ_L and λ_S are non-negative weights.

B. Contributions

This work investigates in detail the extension of the L+S model for dynamic data to a Low-rank + Adaptive Sparse SIgnal (LASSI) model. In particular, we decompose the underlying temporal image sequence into a low-rank component and a component whose overlapping spatiotemporal (3D) patches are assumed sparse in some *adaptive* dictionary domain[2]. We propose a framework to jointly estimate the underlying signal components and the

[1] We focus on 2D + time for simplicity but the concepts generalize readily to 3D + time.

[2] The LASSI method differs from the scheme in [51] that is not (overlapping) patch-based and involves only a 2D (spatial) dictionary. The model in [51] is that $R_1(x_S) = DZ$ with sparse Z and the atoms of D have size $N_x N_y$ (typically very large). Since often $N_t < N_x N_y$, one can easily construct trivial (degenerate) sparsifying dictionaries (e.g., $D = R_1(x_S)$) in this case. On the other hand, in our framework, the dictionaries are for small spatiotemporal patches, and there are many such overlapping patches for a dynamic image sequence to enable the learning of rich models that capture local spatiotemporal properties.

spatiotemporal dictionary from limited measurements. We compare using ℓ_0 and ℓ_1 penalties for sparsity in our formulations, and also investigate adapting structured dictionaries, where the atoms of the dictionary, after being reshaped into space-time matrices are low-rank. The proposed iterative LASSI reconstruction algorithms involve efficient block coordinate descent-type updates of the dictionary and sparse coefficients of patches, and an efficient proximal gradient-based update of the signal components. We also obtain novel sparsity penalized dictionary-blind compressed sensing methods as special cases of our LASSI approaches.

Our experiments demonstrate the promising performance of the proposed data-driven schemes for dMRI reconstruction from limited k-t space data. In particular, we show that the LASSI methods give much improved reconstructions compared to the recent L+S method and methods involving joint L & S modeling [47]. We also show improvements with LASSI compared to the proposed spatiotemporal dictionary-BCS methods (that are special cases of LASSI). Moreover, learning structured dictionaries and using the ℓ_0 sparsity "norm" in LASSI are shown to be advantageous in practice. Finally, in our experiments, we compare the use of conventional singular value thresholding (SVT) for updating the low-rank signal component in the LASSI algorithms to alternative approaches including the recent OptShrink method [52]–[54].

A short version of this work investigating a specific LASSI method appears elsewhere [55]. Unlike [55], here, we study several dynamic signal models and reconstruction approaches in detail, and illustrate the convergence and learning behavior of the proposed methods, and demonstrate their effectiveness for several datasets and undersampling factors.

C. Organization

The rest of this paper is organized as follows. Section II describes our models and problem formulations for dynamic image reconstruction. Section III presents efficient algorithms for the proposed problems and discusses the algorithms' properties. Section IV presents experimental results demonstrating the convergence behavior and performance of the proposed schemes for the dynamic MRI application. Section V concludes with proposals for future work.

II. Models and Problem Formulations

A. LASSI Formulations

We model the dynamic image data as $x = x_L + x_S$, where x_L is low-rank when reshaped into a (space-time) matrix, and we assume that the spatiotemporal (3D) patches in the vectorized tensor x_S are sparse in some adaptive dictionary domain. We replace the regularizer $\zeta(x_s) = \| Tx_S \|_1$ with weight λ_S in (P0) with the following patch-based dictionary learning regularizer

$$\begin{aligned} \zeta(x_s) = \min_{D,Z} \sum_{j=1}^{M} \|P_j x_S - D z_j\|_2^2 + \lambda_Z^2 \|Z\|_0 \\ \text{s. t.} \quad \|Z\|_\infty \leq a, \ \text{rank}\,(R_2(d_i)) \leq r, \ \ \|d_i\|_2 = 1 \forall i \end{aligned} \quad (1)$$

to arrive at the following problem for joint image sequence reconstruction and dictionary estimation:

$$\begin{aligned} \min_{D,Z,x_L,x_S} \ & \tfrac{1}{2}\|A(x_L+x_S)-d\|_2^2+\lambda_L\|R_1(x_L)\|_* \\ & +\lambda_S\left\{\textstyle\sum_{j=1}^{M}\|P_j x_S-Dz_j\|_2^2+\lambda_Z^2\|Z\|_0\right\} \\ \text{s. t.} \ & \|Z\|_\infty \le a, \ \operatorname{rank}(R_2(d_i)) \le r, \ \|d_i\|_2=1 \forall i. \end{aligned} \quad \text{(P1)}$$

Here, P_j is a patch extraction matrix that extracts an $m_x \times m_y \times m_t$ spatiotemporal patch from x_S as a vector. A total of M (spatially and temporally) overlapping 3D patches are assumed. Matrix $D \in \mathbb{C}^{m \times K}$ with $m = m_x m_y m_t$ is the synthesis dictionary to be learned and $z_j \in \mathbb{C}^K$ is the unknown sparse code for the jth patch, with $P_j x_S \approx Dz_j$.

We use $Z \in \mathbb{C}^{K \times M}$ to denote the matrix that has the sparse codes z_j as its columns, $\|Z\|_0$ (based on the ℓ_0 "norm") counts the number of nonzeros in the matrix Z, and $\lambda_Z \ge 0$. Problem (P1) penalizes the number of nonzeros in the (entire) coefficient matrix Z, allowing variable sparsity levels across patches. This is a general and flexible model for image patches (e.g., patches from different regions in the dynamic image sequence may contain different amounts of information and therefore all patches may not be well represented at the same sparsity) and leads to promising performance in our experiments. The constraint $\|Z\|_\infty \triangleq \max_j \|z_j\|_\infty \le a$ with $a > 0$ is used in (P1) because the objective (specifically the regularizer (1)) is non-coercive with respect to Z [56]. [3] The ℓ_∞ constraint prevents pathologies that could theoretically arise (e.g., unbounded algorithm iterates) due to the non-coercive objective. In practice, we set a very large, and the constraint is typically inactive.

The atoms or columns of D, denoted by d_i, are constrained to have unit norm in (P1) to avoid scaling ambiguity between D and Z [56], [57]. We also model the reshaped dictionary atoms $R_2(d_i)$ as having rank at most $r > 0$, where the operator $R_2(\cdot)$ reshapes d_i into a $m_x m_y \times m_t$ space-time matrix. Imposing low-rank (small r) structure on reshaped dictionary atoms is motivated by our empirical observation that the dictionaries learned on image patches (without such a constraint) tend to have reshaped atoms with only a few dominant singular values. Results included in the supplement[4] show that dictionaries learned on dynamic image patches with low-rank atom constraints tend to represent such data as well as learned dictionaries with full-rank atoms. Importantly, such structured dictionary learning may be less prone to over-fitting in scenarios involving limited or corrupted data. We illustrate this for the dynamic MRI application in Section IV.

When z_j is highly sparse (with $\|z_j\|_0 \ll \min(m_t, m_x m_y)$) and $R_2(d_i)$ has low rank (say rank-1), the model $P_j x_S \approx Dz_j$ corresponds to approximating the space-time patch matrix as a sum of a few reshaped low-rank (rank-1) atoms. This special (extreme) case would correspond to approximating the patch itself as low-rank. However, in general the decomposition Dz_j could

[3] Such a non-coercive function remains finite even in cases when $\|Z\| \to \infty$. For example, consider a dictionary D that has a column d_i that repeats. Then, in this case, the patch coefficient vector z_j in (P1) could have entries α and $-\alpha$ respectively, corresponding to the two repeated atoms in D, and the objective would be invariant to arbitrarily large scaling of $|\alpha|$ (i.e., non-coercive).

[4] Supplementary material is available in the supplementary files/multimedia tab.

involve numerous ($> \min(m_t, m_x m_y)$) active atoms, corresponding to a rich, not necessarily low-rank, patch model. Experimental results in Section IV illustrate the benefits of such rich models.

Problem (P1) jointly learns a decomposition $x = x_L + x_S$ and a dictionary D along with the sparse coefficients Z (of spatiotemporal patches) from the measurements d. Unlike (P0), the fully-adaptive Problem (P1) is nonconvex. An alternative to (P1) involves replacing the ℓ_0 "norm" with the convex ℓ_1 norm (with $\|Z\|_1 = \sum_{j=1}^{M} \|z_j\|_1$) as follows:

$$\begin{aligned} &\min_{D,Z,x_L,x_S} \tfrac{1}{2}\|A(x_L + x_S) - d\|_2^2 + \lambda_L \|R_1(x_L)\|_* \\ &+ \lambda_S \left\{ \textstyle\sum_{j=1}^{M} \|P_j x_S - D z_j\|_2^2 + \lambda_Z \|Z\|_1 \right\} \\ &\text{s. t.} \quad \|Z\|_\infty \leq a, \ \operatorname{rank}(R_2(d_i)) \leq r, \ \ \|d_i\|_2 = 1 \forall i. \end{aligned} \tag{P2}$$

Problem (P2) is also nonconvex due to the product Dz_j (and the nonconvex constraints), so the question of choosing (P2) or (P1) is one of image quality, not convexity.

Finally, the convex nuclear norm penalty $\|R_1(x_L)\|_*$ in (P1) or (P2) could be alternatively replaced with a nonconvex penalty on the rank of $R_1(x_L)$, or the function $\|\cdot\|_p^p$ for $p < 1$ (based on the Schatten p-norm) that is applied to the vector of singular values of $R_1(x_L)$ [47]. While we focus mainly on the popular nuclear norm penalty in our investigations, we also briefly study some of the alternatives in Section III and Section IV-D.

B. Special Case of LASSI Formulations: Dictionary-Blind Image Reconstruction

When $\lambda_L \to \infty$ in (P1) or (P2), the optimal low-rank component of the dynamic image sequence becomes inactive (zero). The problems then become pure spatiotemporal dictionary-blind image reconstruction problems (with $x_L = 0$ and $x = x_S$) involving ℓ_0 or ℓ_1 overall sparsity [56] penalties. For example, Problem (P1) reduces to the following form:

$$\begin{aligned} &\min_{D,Z,x} \tfrac{1}{2}\|Ax - d\|_2^2 + \lambda_S \left\{ \textstyle\sum_{j=1}^{M} \|P_j x - D z_j\|_2^2 + \lambda_Z^2 \|Z\|_0 \right\} \\ &\text{s. t.} \quad \|Z\|_\infty \leq a, \ \operatorname{rank}(R_2(d_i)) \leq r, \ \ \|d_i\|_2 = 1 \forall i. \end{aligned} \tag{2}$$

We refer to formulation (2) with its low-rank atom constraints as the DINO-KAT (DIctioNary with lOw-ranK AToms) blind image reconstruction problem. A similar formulation is obtained from (P2) but with an ℓ_1 penalty. These formulations differ from the ones proposed for dynamic image reconstruction in prior works such as [28], [35], [31]. In [35], dynamic image reconstruction is performed by learning a common real-valued dictionary for the spatio-temporal patches of the real and imaginary parts of the dynamic image sequence. The algorithm therein involves dictionary learning using K-SVD [21], where sparse coding is performed using the approximate and expensive orthogonal matching pursuit method [58]. In contrast, the algorithms in this work (cf. Section III) for the overall sparsity penalized DINO-KAT blind image reconstruction problems involve simple and efficient updating of the *complex-valued* spatio-temporal dictionary (for complex-valued 3D

patches) and sparse coefficients (by simple thresholding) in the formulations. The advantages of employing sparsity penalized dictionary learning over conventional approaches like K-SVD are discussed in more detail elsewhere [56]. In [31], a spatio-temporal dictionary is learned for the complex-valued 3D patches of the dynamic image sequence (a total variation penalty is also used), but the method again involves dictionary learning using K-SVD. In the blind compressed sensing method of [28], the time-profiles of individual image pixels were modeled as sparse in a learned dictionary. The 1D voxel time-profiles are a special case of general overlapping 3D (spatio-temporal) patches. Spatio-temporal dictionaries as used here may help capture redundancies in both spatial and temporal dimensions in the data. Finally, unlike the prior works, the DINO-KAT schemes in this work involve structured dictionary learning with low-rank reshaped atoms.

III. Algorithms and Properties

A. Algorithms

We propose efficient block coordinate descent-type algorithms for (P1) and (P2), where, in one step, we update (D,Z) keeping (x_L, x_S) fixed (*Dictionary Learning Step*), and then we update (x_L, x_S) keeping (D,Z) fixed (*Image Reconstruction Step*). We repeat these alternating steps in an iterative manner. The algorithm for the DINO-KAT blind image reconstruction problem (2) (or its ℓ_1 version) is similar, except that $x_L = 0$ during the update steps. Therefore, we focus on the algorithms for (P1) and (P2) in the following.

1) Dictionary Learning Step—Here, we optimize (P1) or (P2) with respect to (D,Z). We first describe the update procedure for (P1). Denoting by P the matrix that has the patches $P_j x_S$ for $1 \leq j \leq M$ as its columns, and with $C \triangleq Z^H$, the optimization problem with respect to (D,Z) in the case of (P1) can be rewritten as follows:

$$\min_{D,C} \ \|P - DC^H\|_F^2 + \lambda_Z^2 \|C\|_0 \quad \text{s. t.} \quad \|C\|_\infty \leq a, \ \operatorname{rank}(R_2(d_i)) \leq r, \ \|d_i\|_2 = 1 \forall i. \tag{P3}$$

Here, we express the matrix DC^H as a Sum of OUter Products (SOUP) $\sum_{i=1}^{K} d_i c_i^H$. We then employ an iterative block coordinate descent method for (P3), where the columns c_i of C and atoms d_i of D are updated sequentially by cycling over all i values [56]. Specifically, for each $1 \leq i \leq K$, we solve (P3) first with respect to c_i (*sparse coding*) and then with respect to d_i (*dictionary atom update*).

For the minimization with respect to c_i, we have the following subproblem, where $E_i \triangleq P - \sum_{k \neq i} d_k c_k^H$ is computed using the most recent estimates of the other variables:

$$\min_{c_i \in \mathbb{C}^M} \ \|E_i - d_i c_i^H\|_F^2 + \lambda_Z^2 \|c_i\|_0 \ \text{s. t.} \ \ \|c_i\|_\infty \leq a. \tag{3}$$

The minimizer $\hat{c}_i$ of (3) is given by [56]

$$\hat{c}_i = \min\left(|H_{\lambda_z}(E_i^H d_i)|, a1_M\right) \odot e^{j\angle E_i^H d_i}, \quad (4)$$

where the hard-thresholding operator $H_{\lambda_Z}(\cdot)$ zeros out vector entries with magnitude less than λ_Z and leaves the other entries (with magnitude $\geq \lambda_Z$) unaffected. Here, $|\cdot|$ computes the magnitude of vector entries, 1_M denotes a vector of ones of length M, "$\odot$" denotes element-wise multiplication, $\min(\cdot, \cdot)$ denotes element-wise minimum, and we choose a such that $a > \lambda_Z$. For a vector $c \in \mathbb{C}^M$, $e^{j\angle c} \in \mathbb{C}^M$ is computed element-wise, with "$\angle$" denoting the phase.

Optimizing (P3) with respect to the atom d_i while holding all other variables fixed yields the following subproblem:

$$\min_{d_i \in \mathbb{C}^m} \|E_i - d_i c_i^H\|_F^2 \text{ s. t. } \operatorname{rank}(R_2(d_i)) \leq r, \|d_i\|_2 = 1. \quad (5)$$

Let $U_r \sum_r V_r^H$ denote an optimal rank-r approximation to $R_2(E_i c_i) \in \mathbb{C}^{m_x m_y \times m_t}$ that is obtained using the r leading singular vectors and singular values of the full singular value decomposition (SVD) $R_2(E_i c_i) \triangleq U \Sigma V^H$. Then a global minimizer of (5), upon reshaping, is

$$R_2(\hat{d}_i) = \begin{cases} \frac{U_r \sum_r V_r^H}{\|\sum_r\|_F}, & \text{if } c_i \neq 0 \\ W, & \text{if } c_i = 0 \end{cases} \quad (6)$$

where W is any normalized matrix with rank at most r, of appropriate dimensions (e.g., we use the reshaped first column of the $m \times m$ identity matrix). The proof for (6) is included in the supplementary material.

If $r = \min(m_x, m_y, m_t)$, then no SVD is needed and the solution is [56]

$$\hat{d}_i = \begin{cases} \frac{E_i c_i}{\|E_i c_i\|_2}, & \text{if } c_i \neq 0 \\ w, & \text{if } c_i = 0 \end{cases} \quad (7)$$

where w is any vector on the m-dimensional unit sphere (e.g., we use the first column of the $m \times m$ identity).

In the case of (P2), when minimizing with respect to (D, Z), we again set $C = Z^H$, which yields an ℓ_1 penalized dictionary learning problem (a simple variant of (P3)). The dictionary and sparse coefficients are then updated using a similar block coordinate descent method as for (P3). In particular, the coefficients c_i are updated using soft thresholding:

$$\hat{c}_i = \max\left(|E_i^H d_i| - \frac{\lambda_Z}{2} 1_M, 0\right) \odot e^{j\angle E_i^H d_i}. \quad (8)$$

2) Image Reconstruction Step—Minimizing (P1) or (P2) with respect to x_L and x_S yields the following subproblem:

$$\min_{x_L, x_S} \frac{1}{2}\|A(x_L + x_S) - d\|_2^2 + \lambda_L \|R_1(x_L)\|_* + \lambda_S \sum_{j=1}^{M} \|P_j x_S - D z_j\|_2^2. \quad \text{(P4)}$$

Problem (P4) is convex but nonsmooth, and its objective has the form $f(x_L, x_S) + g_1(x_L) + g_2(x_S)$, with $f(x_L, x_S) \triangleq 0.5\|A(x_L + x_S) - d\|_2^2$, $g_1(x_L) \triangleq \lambda_L \|R_1(x_L)\|_*$, and $g_2(x_S) \triangleq \lambda_S \sum_{j=1}^{M} \|P_j x_S - D z_j\|_2^2$. We employ the proximal gradient method [45] for (P4), whose iterates, denoted by superscript k, take the following form:

$$x_L^k = \text{prox}_{t_k g_1}(x_L^{k-1} - t_k \nabla_{x_L} f(x_L^{k-1}, x_S^{k-1})), \quad (9)$$

$$x_S^k = \text{prox}_{t_k g_2}(x_S^{k-1} - t_k \nabla_{x_S} f(x_L^{k-1}, x_S^{k-1})), \quad (10)$$

where the proximity function is defined as

$$\text{prox}_{t_k g}(y) = \arg\min_z \frac{1}{2}\|y - z\|_2^2 + t_k\, g(z), \quad (11)$$

and the gradients of f are given by

$$\nabla_{x_L} f(x_L, x_S) = \nabla_{x_S} f(x_L, x_S) = A^H A(x_L + x_S) - A^H d.$$

The update in (9) corresponds to the singular value thresholding (SVT) operation [59]. Indeed, defining $\tilde{x}_L^{k-1} \triangleq x_L^{k-1} - t_k \nabla_{x_L} f(x_L^{k-1}, x_S^{k-1})$, it follows from (9) and (11) [59] that

$$R_1(x_L^k) = \mathbf{SVT}_{t_k \lambda_L}(R_1(\tilde{x}_L^{k-1})). \quad (12)$$

Here, the SVT operator for a given threshold $\tau > 0$ is

$$\mathbf{SVT}_{\tau}(Y) = \sum_{i} (\sigma_i - \tau)^{+} u_i v_i^H, \tag{13}$$

where $U\Sigma V^H$ is the SVD of Y with σ_i denoting the ith largest singular value and u_i and v_i denoting the ith columns of U and V, and $(\cdot)^+ = \max(\cdot, 0)$ sets negative values to zero.

Let $\tilde{x}_S^{k-1} \triangleq x_S^{k-1} - t_k \nabla_{x_S} f(x_L^{k-1}, x_S^{k-1})$. Then (10) and (11) imply that x_S^k satisfies the following Normal equation:

$$\left(I + 2t_k \lambda_S \sum_{j=1}^{M} P_j^T P_j \right) x_S^k = \tilde{x}_S^{k-1} + 2t_k \lambda_S \sum_{j=1}^{M} P_j^T D z_j. \tag{14}$$

Solving (14) for x_S^k is straightforward because the matrix pre-multiplying x_S^k is diagonal, and thus its inverse can be computed cheaply. The term $2t_k \lambda_S \sum_{j=1}^{M} P_j^T D z_j$ in (14) can also be computed cheaply using patch-based operations.

The proximal gradient method for (P4) converges [60] for a constant step-size $t_k = t < 2/\ell$, where ℓ is the Lipschitz constant of $\nabla f(x_L, x_S)$. For (P4), $\ell = 2\|A\|_2^2$. In practice, ℓ can be precomputed using standard techniques such as the power iteration method. In our dMRI experiments in Section IV, we normalize the encoding operator A so that $\|A\|_2 = 1$ for fully-sampled measurements (cf. [45], [61]) to ensure that $\|A\|_2^2 \leq 1$ in undersampled (k-t space) scenarios.

When the nuclear norm penalty in (P4) is replaced with a rank penalty, i.e., $g_1(x_L) \triangleq \lambda_L \text{rank}(R_1(x_L))$, the proximity function is a modified form of the SVT operation in (12) (or (13)), where the singular values smaller than $\sqrt{2t_k\lambda_L}$ are set to zero and the other singular values are left unaffected (i.e., hard-thresholding the singular values). Alternatively, when the nuclear norm penalty is replaced with $\|\cdot\|_p^p$ (for $p < 1$) applied to the vector of singular values of $R_1(x_L)$ [47], the proximity function can still be computed cheaply when $p = 1/2$ or $p = 2/3$, for which the soft thresholding of singular values in (13) is replaced with the solution of an appropriate polynomial equation (see [62]). For general p, the x_L update could be performed using strategies such as in [47].

The nuclear norm-based low-rank regularizer $\|R_1(x_L)\|_*$ is popular because it is the tightest convex relaxation of the (nonconvex) matrix rank penalty. However, this does not guarantee that the nuclear norm (or its alternatives) is the optimal (in any sense) low-rank regularizer in practice. Indeed, the argument $R_1(\tilde{x}_L^{k-1})$ of the SVT operator in (12) can be interpreted as an estimate of the underlying (true) low-rank matrix $R_1(x_L)$ plus a residual (noise) matrix. In [52], the low-rank denoising problem was studied from a random-matrix-theoretic perspective and an algorithm – OptShrink – was derived that asymptotically achieves

minimum squared error among all estimators that shrink the singular values of their argument. We leverage this result for dMRI by proposing the following modification of (12):

$$R_1(x_L^k) = \mathbf{OptShrink}_{r_L}(R_1(\tilde{x}_L^{k-1})). \quad (15)$$

Here, $\mathbf{OptShrink}_{r_L}(.)$ is the data-driven OptShrink estimator from Algorithm 1 of [52] (see the supplementary material for more details and discussion of OptShrink). In this variation, the regularization parameter λ_L is replaced by a parameter $r_L \in \mathbb{N}$ that directly specifies the rank of $R_1(x_L^k)$, and the (optimal) shrinkage for each of the leading r_L singular values is implicitly estimated based on the distribution of the remaining singular values. Intuitively, we expect this variation of the aforementioned (SVT-based) proximal gradient scheme to yield better estimates of the underlying low-rank component of the reconstruction because, at each iteration k (in (9)), the OptShrink-based update (15) should produce an estimate of the underlying low-rank matrix $R_1(x_L)$ with smaller squared error than the corresponding SVT-based update (12). Similar OptShrink-based schemes have shown promise in practice [53], [54]. In particular, in [53] it is shown that replacing the SVT-based low-rank updates in the algorithm [45] for (P0) with OptShrink updates can improve dMRI reconstruction quality. In practice, small r_L values perform well due to the high spatio-temporal correlation of the background in dMRI.

Fig. 1 shows the LASSI reconstruction algorithms for Problems (P1) and (P2), respectively. As discussed, we can obtain variants of these proposed LASSI algorithms by replacing the SVT-based x_L update (12) in the image reconstruction step with an OptShrink-based update (15), or with the update arising from the rank penalty or from the Schatten p-norm ($p < 1$) penalty. The proposed LASSI algorithms start with an initial (x_L^0, x_S^0, D^0, Z^0). For example, D^0 can be set to an analytical dictionary, $Z^0 = 0$, and x_L^0 and x_S^0 could be (for example) set based on some iterations of the recent L+S method [45]. In the case of Problem (2), the proposed algorithm is an efficient SOUP-based image reconstruction algorithm. We refer to it as the DINO-KAT image reconstruction algorithm in this case.

B. Convergence and Computational Cost

The proposed LASSI algorithms for (P1) and (P2) alternate between updating (D,Z) and (x_L, x_S). Since we update the dictionary atoms and sparse coefficients using an exact block coordinate descent approach, the objectives in our formulations only decrease in this step. When the (x_L, x_S) update is performed using proximal gradients (which is guaranteed to converge to the global minimizer of (P4)), by appropriate choice of the constant-step size [63], the objective functions can be ensured to be monotone (non-increasing) in this step. Thus, the costs in our algorithms are monotone decreasing, and because they are lower-bounded (by 0), they must converge. Whether the iterates in the LASSI algorithms converge to the critical points [64] in (P1) or (P2) [56] is an interesting question that we leave for future work.

In practice, the computational cost per outer iteration of the proposed algorithms is dominated by the cost of the dictionary learning step, which scales (assuming $K \propto m$ and $M \propto K,m$) as $O(m^2MJ)$, where J is the number of times the matrix D is updated in the dictionary learning step. The SOUP dictionary learning cost is itself dominated by various matrix-vector products, whereas the costs of the truncated hard-thresholding (4) and low-rank approximation (6) steps are negligible. On the other hand, when dictionary learning is performed using methods like K-SVD [21] (e.g., in [18], [30]), the associated cost (assuming per-patch sparsity $\propto m$) may scale worse[5] as $O(m^3MJ)$. Section IV illustrates that our algorithms converge quickly in practice.

IV. Numerical Experiments

A. Framework

The proposed LASSI framework can be used for inverse problems involving dynamic data, such as in dMRI, interventional imaging, video processing, etc. Here, we illustrate the convergence behavior and performance of our methods for dMRI reconstruction from limited k-t space data. Section IV-B focuses on empirical convergence and learning behavior of the methods. Section IV-C compares the image reconstruction quality obtained with LASSI to that obtained with recent techniques. Section IV-D investigates and compares the various LASSI models and methods in detail. We compare using the ℓ_0 "norm" (i.e., (P1)) to the ℓ_1 norm (i.e., (P2)), structured (with low-rank atoms) dictionary learning to the learning of unstructured (with full-rank atoms) dictionaries, and singular value thresholding-based x_L update to OptShrink-based or other alternative x_L updates in LASSI. We also investigate the effects of the sparsity level (i.e., number of nonzeros) of the learned Z and the overcompleteness of D in LASSI, and demonstrate the advantages of adapting the patch-based LASSI dictionary compared to using fixed dictionary models in the LASSI algorithms. The LASSI methods are also shown to perform well for various initializations of x_L and x_S.

We work with several dMRI datasets from prior works [45], [47]: 1) the Cartesian cardiac perfusion data [45], [61], 2) a 2D cross section of the physiologically improved nonuniform cardiac torso (PINCAT) [65] phantom data (see [47], [66]), and 3) the *in vivo* myocardial perfusion MRI data in [47], [66]. The cardiac perfusion data were acquired with a modified TurboFLASH sequence on a 3T scanner using a 12-element coil array. The fully sampled data with an image matrix size of 128×128 (128 phase encode lines) and 40 temporal frames was acquired with FOV = 320 × 320 mm^2, slice thickness = 8 mm, spatial resolution = 3.2 mm^2, and temporal resolution of 307 ms [45]. The coil sensitivity maps are provided in [61]. The (single coil) PINCAT data (as in [66]) had image matrix size of 128 × 128 and 50 temporal frames. The single coil *in vivo* myocardial perfusion data was acquired on a 3T scanner using a saturation recovery FLASH sequence with Cartesian sampling (TR/TE = 2.5/1 ms, saturation recovery time = 100 ms), and had a image matrix size of 90×190 (phase encodes × frequency encodes) and 70 temporal frames [47].

[5] In [56], we have shown that efficient SOUP learning-based image reconstruction methods outperform methods based on K-SVD in practice.

Fully sampled data (PINCAT and *in vivo* data were normalized to unit peak image intensity, and the cardiac perfusion data [45] had a peak image intensity of 1.27) were retrospectively undersampled in our experiments. We used Cartesian and pseudo-radial undersampling patterns. In the case of Cartesian sampling, we used a different variable-density random Cartesian undersampling pattern for each time frame. The pseudo-radial (sampling radially at uniformly spaced angles for each time frame and with a small random rotation of the radial lines between frames) sampling patterns were obtained by subsampling on a Cartesian grid for each time frame. We simulate several undersampling (acceleration) factors of k-t space in our experiments. We measure the quality of the dMRI reconstructions using the normalized root mean square error (NRMSE) metric defined as $\|x_{\text{recon}} - x_{\text{ref}}\|_2 / \|x_{\text{ref}}\|_2$, where x_{ref} is a reference reconstruction from fully sampled data, and x_{recon} is the reconstruction from undersampled data.

We compare the quality of reconstructions obtained with the proposed LASSI methods to those obtained with the recent L+S method [45] and the k-t SLR method involving joint L & S modeling [47]. For the L+S and k-t SLR methods, we used the publicly available MATLAB implementations [61], [66]. We chose the parameters for both methods (e.g., λ_L and λ_S for L+S in (P0) or λ_1, λ_2, etc. for k-t SLR [47], [66]) by sweeping over a range of values and choosing the settings that achieved good NRMSE in our experiments. We optimized parameters separately for each dataset to achieve the lowest NRMSE at some intermediate undersampling factors, and observed that these settings also worked well at other undersampling factors. The L+S method was simulated for 250 iterations and k-t SLR was also simulated for sufficient iterations to ensure convergence. The operator T (in (P0)) for L+S was set to a temporal Fourier transform, and a total variation sparsifying penalty (together with a nuclear norm penalty for enforcing low-rankness) was used in k-t SLR. The dynamic image sequence in both methods was initialized with a baseline reconstruction (for the L+S method, L was initialized with this baseline and S with zero) that was obtained by first performing zeroth order interpolation at the nonsampled k-t space locations (by filling in with the nearest non-zero entry along time) and then backpropagating the filled k-t space to image space (i.e., pre-multiplying by the A^H corresponding to fully sampled data).

For the LASSI method, we extracted spatiotemporal patches of size $8 \times 8 \times 5$ from x_S in (P1) with spatial and temporal patch overlap strides of 2 pixels.[6] The dictionary atoms were reshaped into 64×5 space-time matrices, and we set the rank parameter $r = 1$, except for the invivo dataset [47], [66], where we set $r = 5$. We ran LASSI for 50 outer iterations with 1 and 5 inner iterations in the (D,Z) and (x_L, x_S) updates, respectively. Since Problem (P1) is nonconvex, the proposed algorithm needs to be initialized appropriately. We set the initial $Z = 0$, and the initial x_L and x_S were typically set based on the outputs of either the L+S or k-t SLR methods. When learning a square dictionary, we initialized D with a 320×320 DCT, and, in the overcomplete ($K > m$) case, we concatenated the square DCT initialization with normalized and vectorized patches that were selected from random locations of the initial reconstruction. We empirically show in Section IV-D that the proposed LASSI algorithms typically improve image reconstruction quality compared to that achieved by their

[6]While we used a stride of 2 pixels, a spatial and temporal patch overlap stride of 1 pixel would further enhance the reconstruction performance of LASSI in our experiments, but at the cost of substantially more computation.

initializations. We selected the weights λ_L, λ_S, and λ_Z for the LASSI methods separately for each dataset by sweeping over a range (3D grid) of values and picking the settings that achieved the lowest NRMSE at intermediate undersampling factors (as for L+S and k-t SLR) in our experiments. These tuned parameters also worked well at other undersampling factors (e.g., see Fig. 5(h)), and are included in the supplement for completeness.

We also evaluate the proposed variant of LASSI involving only spatiotemporal dictionary learning (i.e., dictionary blind compressed sensing). We refer to this method as DINOKAT dMRI, with $r = 1$. We use an ℓ_0 sparsity penalty for DINO-KAT dMRI (i.e., we solve Problem (2)) in our experiments, and the other parameters are set or optimized (cf. the supplement) similarly as described above for LASSI.

The LASSI and DINO-KAT dMRI implementations were coded in Matlab R2016a. Our current Matlab implementations are not optimized for efficiency. Hence, here we perform our comparisons to recent methods based on reconstruction quality (NRMSE) rather than runtimes, since the latter are highly implementation dependant. A link to software to reproduce our results will be provided at http://web.eecs.umich.edu/~fessler/.

B. LASSI Convergence and Learning Behavior

Here, we consider the fully sampled cardiac perfusion data in [45], [61] and perform eight fold Cartesian undersampling of k-t space. We study the behavior of the proposed LASSI algorithms for reconstructing the dMRI data from (multicoil) undersampled measurements. We consider four different LASSI algorithms in our study here: the algorithms for (P1) (with ℓ_0 "norm") and (P2) (with ℓ_1 norm) with SVT-based x_L update; and the variants of these two algorithms where the SVT update step is replaced with an OptShrink (OPT)- type update. The other variants of the SVT update including hard thresholding of singular values or updating based on the Schatten p-norm are studied later in Section IV-D. We learned 320 × 320 dictionaries (with atoms reshaped by the operator $R_2(\cdot)$ into 64 × 5 space-time matrices) for the patches of x_S with $r = 1$, and x_L and x_S were initialized using the corresponding components of the L+S method with $\lambda_L = 1.2$ and $\lambda_S = 0.01$ in (P0) [45]. Here, we jointly tuned λ_L, λ_S, and λ_Z for each LASSI variation, to achieve the best NRMSE.

Fig. 2 shows the behavior of the proposed LASSI reconstruction methods. The objective function values (Fig. 2(a)) in (P1) and (P2) decreased monotonically and quickly for the algorithms with SVT-based x_L update. The OptShrink-based x_L update does not correspond to minimizing a formal cost function, so the OPT-based algorithms are omitted in Fig. 2(a). All four LASSI methods improved the NRMSE over iterations compared to the initialization. The NRMSE converged (Fig. 2(b)) in all four cases, with the ℓ_0 "norm"-based methods outperforming the ℓ_1 penalty methods. Moreover, when employing the ℓ_0 sparsity penalty, the OPT-based method ($r_L = 1$) outperformed the SVT-based one for the dataset. The sparsity fraction ($\|Z\|_0 / mM$) for the learned coefficients matrix (Fig. 2(c)) converged to small values (about 10–20 %) in all cases indicating that highly sparse representations are obtained in the LASSI models. Lastly, the difference between successive dMRI reconstructions (Fig. 2(d)) quickly decreased to small values, suggesting iterate convergence.

Figs. 2(g) and (h) show the reconstructions[7] and x_L and x_S components of two representative frames produced by the L+S [45] (with parameters optimized to achieve best NRMSE) and LASSI (OPT update and ℓ_0 sparsity) methods, respectively. The LASSI reconstructions are sharper and a better approximation of the reference frames (fully sampled reconstructions) shown. In particular, the x_L component of the LASSI reconstruction is clearly low-rank, and the x_S component captures the changes in contrast and other dynamic features in the data. On the other hand, the x_L component of the conventional L+S reconstruction varies more over time (i.e., it has higher rank), and the x_S component contains relatively little information. The richer (x_L, x_S) decomposition produced by LASSI suggests that both the low-rank and adaptive dictionary-sparse components of the model are well-suited for dMRI.

Figs. 2(e) and (f) show the real and imaginary parts of the atoms of the learned D in LASSI with OptShrink-based x_L updating and ℓ_0 sparsity. Only the first columns (time-point) of the (rank-1) reshaped 64×5 atoms are shown as 8×8 patches. The learned atoms contain rich geometric and frequency-like structures that were jointly learned with the dynamic signal components from limited k-t space measurements.

C. Dynamic MRI Results and Comparisons

Here, we consider the fully sampled cardiac perfusion data [45], [61], PINCAT data [47], [66], and *in vivo* myocardial perfusion data [47], [66], and simulate k-t space undersampling at various acceleration factors. Cartesian sampling was used for the first dataset, and pseudo-radial sampling was employed for the other two. The performance of LASSI and DINO-KAT dMRI is compared to that of L+S [45] and k-t SLR [47]. The LASSI and DINO-KAT dMRI algorithms were simulated with an ℓ_0 sparsity penalty and a 320×320 dictionary. OptShrink-based x_L updates were employed in LASSI for the cardiac perfusion data, and SVT-based updates were used in the other cases. For the cardiac perfusion data, the initial x_L and x_S in LASSI were from the L+S framework [45] (and the initial x in DINO-KAT dMRI was an L+S dMRI reconstruction). For the PINCAT and *in vivo* myocardial perfusion data, the initial x_S in LASSI (or x in DINO-KAT dMRI) was the (better) k-t SLR reconstruction and the initial x_L was zero. All other settings are as discussed in Section IV-A.

Tables I, II and III list the reconstruction NRMSE values for LASSI, DINO-KAT dMRI, L+S [45] and k-t SLR [47] for the cardiac perfusion, PINCAT, and *in vivo* datasets, respectively. The LASSI method provides the best NRMSE values, and the proposed DINO-KAT dMRI method also outperforms the prior L+S and k-t SLR methods. The NRMSE gains achieved by LASSI over the other methods are indicated in the tables for each dataset and undersampling factor. The LASSI framework provides an average improvement of 1.9 dB, 1.5 dB, and 0.5 dB respectively, over the L+S, k-t SLR, and (proposed) DINO-KAT dMRI methods. This suggests the suitability of the richer LASSI model for dynamic image sequences compared to the jointly low-rank and sparse (k-t SLR), low-rank plus nonadaptive sparse (L+S), and purely adaptive dictionary-sparse (DINO-KAT dMRI) signal models.

It is often of interest to compute the reconstruction NRMSE over a region of interest (ROI) containing the heart. Additional tables included in the supplement show the reconstruction

[7]Gamma correction was used to better display the images in this work.

NRMSE values computed over such ROIs for LASSI, DINOKAT dMRI, L+S, and k-t SLR for the cardiac perfusion, PINCAT, and *in vivo* datasets. The proposed LASSI and DINO-KAT dMRI methods provide much lower NRMSE in the heart ROIs compared to the other methods.

Fig. 3 shows the NRMSE values computed between each reconstructed and reference frame for the LASSI, L+S, and k-t SLR outputs for two datasets. The proposed LASSI scheme clearly outperforms the previous L+S and k-t SLR methods across frames (time). Fig. 4 shows the LASSI reconstructions of some representative frames (the supplement shows more such reconstructions) for each dataset in Tables I-III. The reconstructed frames are visually similar to the reference frames (fully sampled reconstructions) shown. Fig. 4 also shows the reconstruction error maps (i.e., the magnitude of the difference between the magnitudes of the reconstructed and reference frames) for LASSI, L+S, and k-t SLR for the representative frames of each dataset. The error maps for LASSI show fewer artifacts and smaller distortions than the other methods. Results included in the supplement show that LASSI recovers temporal (x–t) profiles in the dynamic data with greater fidelity than other methods.

D. A Study of Various LASSI Models and Methods

Here, we investigate the various LASSI models and methods in detail. We work with the cardiac perfusion data [45] and simulate the reconstruction performance of LASSI for Cartesian sampling at various undersampling factors. Unless otherwise stated, we simulate LASSI here with the ℓ_0 sparsity penalty, the SVT-based x_L update, $r = 1$, an initial 320×320 (1D) DCT dictionary, and x_S initialized with the dMRI reconstruction from the L+S method [45] and x_L initialized to zero. In the following, we first compare SVT-based updating of x_L to alternatives in the algorithms and the use of ℓ_0 versus ℓ_1 sparsity penalties. The weights λ_L, λ_S, and λ_Z were tuned for each LASSI variation. Second, we study the behavior of LASSI for different initializations of the underlying signal components or dictionary. Third, we study the effect of the number of atoms of D on LASSI performance. Fourth, we study the effect of the sparsity level of the learned Z on the reconstruction quality in LASSI. Lastly, we study the effect of the atom rank parameter r in LASSI.

1) SVT vs. Alternatives and ℓ_0 vs. ℓ_1 patch sparsity—Figs. 5(a) and (b) show the behavior of the LASSI algorithms using ℓ_0 and ℓ_1 sparsity penalties, respectively. In each case, the results obtained with x_L updates based on SVT, Opt- Shrink (OPT), or based on the Schatten p-norm ($p = 0.5$), and rank penalty are shown. The OptShrink-based singular value shrinkage (with $r_L = 1$) and Schatten p-norm-based shrinkage typically outperform the conventional SVT (based on nuclear norm penalty) as well as the hard thresholding of singular values (for rank penalty) for the cardiac perfusion data. The OptShrink and Schatten p-norm-based x_L updates also perform quite similarly at lower undersampling factors, but OptShrink outperforms the latter approach at higher undersampling factors. Moreover, the ℓ_0 "norm"-based methods outperformed the corresponding ℓ_1 norm methods in many cases (with SVT or alternative approaches). These results demonstrate the benefits of appropriate nonconvex regularizers in practice.

2) Effect of Initializations—Here, we explore the behavior of LASSI for different initializations of the dictionary and the dynamic signal components. First, we consider the LASSI algorithm initialized by the L+S and k-t SLR methods as well as with the baseline reconstruction (obtained by performing zeroth order interpolation at the nonsampled k-t space locations and then backpropagating to image space) mentioned in Section IV-A (all other parameters fixed). The reconstructions from the prior methods are used to initialize x_S in LASSI with $x_L^0 = 0$[8]. Figs. 5(c) and (d) show that LASSI significantly improves the dMRI reconstruction quality compared to the initializations at all undersampling factors tested. The baseline reconstructions had high NRMSE values (not shown in Fig. 5) of about 0.5. Importantly, the reconstruction NRMSE for LASSI with the simple baseline initialization (Fig. 5(d)) is comparable to the NRMSE obtained with the more sophisticated k-t SLR initialization. In general, better initializations (for x_L, x_S) in LASSI may lead to a better final NRMSE in practice.

Next, we consider initializing the LASSI method with the following types of dictionaries (all other parameters fixed): a random i.i.d. gaussian matrix with normalized columns, the 320×320 1D DCT, and the separable 3D DCT of size 320× 320. Fig. 5(g) shows that LASSI performs well for each choice of initialization. We also simulated the LASSI algorithm by keeping the dictionary D fixed (but still updating Z) to each of the aforementioned initializations. Importantly, the NRMSE values achieved by the adaptive-dictionary LASSI variations are substantially better than the values achieved by the fixed-dictionary schemes.

3) Effect of Overcompleteness of D—Fig. 5(e) shows the performance (NRMSE) of LASSI for various choices of the umber of atoms (K) in D at several acceleration factors. The weights in (P1) were tuned for each K. As K is increased, the NRMSE initially shows significant improvements (decrease) of more than 1 dB. This is because LASSI learns richer models that provide sparser representations of patches and, hence, better reconstructions. However, for very large K values, the NRMSE saturates or begins to degrade, since it is harder to learn very rich models using limited imaging measurements (without overfitting artifacts).

4) Effect of the Sparsity Level in LASSI—While Section IV-D1 compared the various ways of updating the low-rank signal component in LASSI, here we study the effect of the sparsity level of the learned Z on LASSI performance. In particular, we simulate LASSI at various values of the parameter λ_Z that controls sparsity (all other parameters fixed). Fig. 5(h) shows the NRMSE of LASSI at various sparsity levels of the learned Z and at several acceleration factors. The weight λ_Z decreases from left to right in the plot and the same set of λ_Z values were selected (for the simulation) at the various acceleration factors. Clearly, the best NRMSE values occur around 10–20% sparsity (when 32–64 dictionary atoms are used on the average to represent the reshaped 64×5 space-time patches of x_S), and the NRMSE degrades when the number of nonzeros in Z is either too high (non-sparse) or too

[8]We have also observed that LASSI improves the reconstruction quality over other alternative initializations such as initializing x_L and x_S using corresponding outputs of the L+S framework.

low (when the dictionary model reduces to a low-rank approximation of space-time patches in x_S). This illustrates the effectiveness of the rich sparsity-driven modeling in LASSI[9].

5) Effect of Rank of Reshaped Atoms—Here, we simulate LASSI with (reshaped) atom ranks $r = 1$ (low-rank) and $r = 5$ (full-rank). Fig. 5(f) shows that LASSI with $r = 1$ provides somewhat improved NRMSE values over the $r = 5$ case at several undersampling factors, with larger improvements at higher accelerations. This result suggests that structured (fewer degrees of freedom) dictionary adaptation may be useful in scenarios involving very limited measurements. In practice, the effectiveness of the low-rank model for reshaped dictionary atoms also depends on the properties of the underlying data.

V. Conclusions

In this work, we investigated a novel framework for reconstructing spatiotemporal data from limited measurements. The proposed LASSI framework jointly learns a low-rank and dictionary-sparse decomposition of the underlying dynamic image sequence together with a spatiotemporal dictionary. The proposed algorithms involve simple updates. Our experimental results showed the superior performance of LASSI methods for dynamic MR image reconstruction from limited k-t space data compared to recent works such as L+S and k-t SLR. The LASSI framework also outperformed the proposed efficient dictionary-blind compressed sensing framework (a special case of LASSI) called DINO-KAT dMRI. We also studied and compared various LASSI methods and formulations such as with ℓ_0 or ℓ_1 sparsity penalties, or with low-rank or full-rank reshaped dictionary atoms, or involving singular value thresholding-based optimization versus some alternatives including OptShrink-based optimization. The usefulness of LASSI-based schemes in other inverse problems and image processing applications merits further study. The LASSI schemes involve parameters (like in most regularization-based methods) that need to be set (or tuned) in practice. We leave the study of automating the parameter selection process to future work. The investigation of dynamic image priors that naturally lead to OptShrink-type low-rank updates in the LASSI algorithms is also of interest, but is beyond the scope of this work, and will be presented elsewhere.

Supplementary Material

Refer to Web version on PubMed Central for supplementary material.

Acknowledgments

This work was supported in part by the following grants: ONR grant N00014-15-1-2141, DARPA Young Faculty Award D14AP00086, ARO MURI grants W911NF-11-1-0391 and 2015-05174-05, NIH grants R01 EB023618 and P01 CA 059827, and a UM-SJTU seed grant.

[9]Fig. 5(h) shows that the same λ_Z value is optimal at various accelerations. An intuitive explanation for this is that as the undersampling factor increases, the weighting of the (first) data-fidelity term in (P1) or (P2) decreases (fewer k-t space samples, or rows of the sensing matrix are selected). Thus, even with fixed λ_Z, the relative weighting of the sparsity penalty would increase, creating a stronger sparsity regularization at higher undersampling factors.

References

1. Donoho D. Compressed sensing. IEEE Trans Information Theory. 2006; 52(4):1289–1306.
2. Candès E, Romberg J, Tao T. Robust uncertainty principles: exact signal reconstruction from highly incomplete frequency information. IEEE Trans Information Theory. 2006; 52(2):489–509.
3. Feng P, Bresler Y. Spectrum-blind minimum-rate sampling and reconstruction of multiband signals. ICASSP. 1996; 3:1689– 1692.
4. Bresler Y, Feng P. Spectrum-blind minimum-rate sampling and reconstruction of 2-D multiband signals. Proc 3rd IEEE Int Conf on Image Processing, ICIP'96. 1996:701–704.
5. Lustig M, Donoho D, Pauly J. Sparse MRI: The application of compressed sensing for rapid MR imaging. Magnetic Resonance in Medicine. 2007; 58(6):1182–1195. [PubMed: 17969013]
6. Lustig M, Santos JM, Donoho DL, Pauly JM. k-t SPARSE: High frame rate dynamic MRI exploiting spatio-temporal sparsity. Proc ISMRM. 2006:2420.
7. Trzasko J, Manduca A. Highly undersampled magnetic resonance image reconstruction via homotopic l_0-minimization. IEEE Trans Med Imaging. 2009; 28(1):106–121. [PubMed: 19116193]
8. Kim Y, Nadar MS, Bilgin A. Wavelet-based compressed sensing using gaussian scale mixtures. Proc ISMRM. 2010:4856.
9. Qiu C, Lu W, Vaswani N. Real-time dynamic MR image reconstruction using kalman filtered compressed sensing. Proc IEEE International Conference on Acoustics, Speech and Signal Processing. 2009:393–396.
10. Gamper U, Boesiger P, Kozerke S. Compressed sensing in dynamic MRI. Magnetic Resonance in Medicine. 2008; 59(2):365–373. [PubMed: 18228595]
11. Jung H, Sung K, Nayak KS, Kim EY, Ye JC. k-t FOCUSS: A general compressed sensing framework for high resolution dynamic MRI. Magnetic Resonance in Medicine. 2009; 61(1):103–116. [PubMed: 19097216]
12. Liang D, Liu B, Wang J, Ying L. Accelerating SENSE using compressed sensing. Magnetic Resonance in Medicine. 2009; 62(6):1574–1584. [PubMed: 19785017]
13. Otazo R, Kim D, Axel L, Sodickson DK. Combination of compressed sensing and parallel imaging for highly accelerated first-pass cardiac perfusion MRI. Magnetic Resonance in Medicine. 2010; 64(3):767–776. [PubMed: 20535813]
14. Wu B, Watts R, Millane R, Bones P. An improved approach in applying compressed sensing in parallel MR imaging. Proc ISMRM. 2009:4595.
15. Liu B, Sebert FM, Zou Y, Ying L. SparseSENSE: Randomly-sampled parallel imaging using compressed sensing. Proc ISMRM. 2008:3154.
16. Adluru G, DiBella EVR. Reordering for improved constrained reconstruction from undersampled k-space data. Journal of Biomedical Imaging. 2008; 2008:1–12.
17. Liang ZP. Spatiotemporal imaging with partially separable functions. IEEE International Symposium on Biomedical Imaging: From Nano to Macro. 2007:988–991.
18. Ravishankar S, Bresler Y. MR image reconstruction from highly undersampled k-space data by dictionary learning. IEEE Trans Med Imag. 2011; 30(5):1028–1041.
19. Olshausen BA, Field DJ. Emergence of simple-cell receptive field properties by learning a sparse code for natural images. Nature. 1996; 381(6583):607–609. [PubMed: 8637596]
20. Engan K, Aase S, Hakon-Husoy J. Method of optimal directions for frame design. Proc IEEE International Conference on Acoustics, Speech, and Signal Processing. 1999:2443–2446.
21. Aharon M, Elad M, Bruckstein A. K-SVD: An algorithm for designing overcomplete dictionaries for sparse representation. IEEE Transactions on signal processing. 2006; 54(11):4311–4322.
22. Mairal J, Bach F, Ponce J, Sapiro G. Online learning for matrix factorization and sparse coding. J Mach Learn Res. 2010; 11:19– 60.
23. Elad M, Aharon M. Image denoising via sparse and redundant representations over learned dictionaries. IEEE Trans Image Process. 2006; 15(12):3736–3745. [PubMed: 17153947]
24. Mairal J, Elad M, Sapiro G. Sparse representation for color image restoration. IEEE Trans on Image Processing. 2008; 17(1):53–69.

25. Lu X, Yuan Y, Yan P. Alternatively constrained dictionary learning for image superresolution. IEEE Transactions on Cybernetics. 2014; 44(3):366–377. [PubMed: 23757556]
26. Gleichman S, Eldar YC. Blind compressed sensing. IEEE Transactions on Information Theory. 2011; 57(10):6958–6975.
27. Ravishankar S, Bresler Y. Multiscale dictionary learning for MRI. Proc ISMRM. 2011:2830.
28. Lingala SG, Jacob M. Blind compressive sensing dynamic MRI. IEEE Transactions on Medical Imaging. 2013; 32(6):1132–1145. [PubMed: 23542951]
29. Lingala SG, Jacob M. Blind compressed sensing with sparse dictionaries for accelerated dynamic MRI. 2013 IEEE 10th International Symposium on Biomedical Imaging. 2013:5–8.
30. Wang, Y., Zhou, Y., Ying, L. Undersampled dynamic magnetic resonance imaging using patch-based spatiotemporal dictionaries. 2013 IEEE 10th International Symposium on Biomedical Imaging (ISBI); April 2013; p. 294-297.
31. Wang Y, Ying L. Compressed sensing dynamic cardiac cine mri using learned spatiotemporal dictionary. IEEE Transactions on Biomedical Engineering. 2014; 61(4):1109–1120. [PubMed: 24658236]
32. Caballero, J., Rueckert, D., Hajnal, JV. Medical Image Computing and Computer- Assisted Intervention MICCAI 2012. Vol. 7510. Springer; Berlin Heidelberg: 2012. Dictionary learning and time sparsity in dynamic MRI; p. 256-263.ser. Lecture Notes in Computer Science
33. Huang Y, Paisley J, Lin Q, Ding X, Fu X, Zhang XP. Bayesian nonparametric dictionary learning for compressed sensing MRI. IEEE Trans Image Process. 2014; 23(12):5007–5019. [PubMed: 25265609]
34. Awate SP, DiBella EVR. Spatiotemporal dictionary learning for undersampled dynamic MRI reconstruction via joint frame-based and dictionary-based sparsity. 2012 9th IEEE International Symposium on Biomedical Imaging (ISBI). 2012:318–321.
35. Caballero J, Price AN, Rueckert D, Hajnal JV. Dictionary learning and time sparsity for dynamic MR data reconstruction. IEEE Transactions on Medical Imaging. 2014; 33(4):979–994. [PubMed: 24710166]
36. Wang S, Peng X, Dong P, Ying L, Feng DD, Liang D. Parallel imaging via sparse representation over a learned dictionary. 2015 IEEE 12th International Symposium on Biomedical Imaging (ISBI). 2015:687–690.
37. Haldar JP, Liang ZP. Spatiotemporal imaging with partially separable functions: A matrix recovery approach. IEEE International Symposium on Biomedical Imaging: From Nano to Macro. 2010:716–719.
38. Zhao B, Haldar JP, Brinegar C, Liang ZP. Low rank matrix recovery for real-time cardiac mri. IEEE International Symposium on Biomedical Imaging: From Nano to Macro. 2010:996–999.
39. Pedersen H, Kozerke S, Ringgaard S, Nehrke K, Kim WY. kt pca: Temporally constrained k-t blast reconstruction using principal component analysis. Magnetic Resonance in Medicine. 2009; 62(3): 706–716. [PubMed: 19585603]
40. Trzasko J, Manduca A. Local versus global low-rank promotion in dynamic mri series reconstruction. Proc ISMRM. 2011:4371.
41. Peng Y, Ganesh A, Wright J, Xu W, Ma Y. Rasl: Robust alignment by sparse and low-rank decomposition for linearly correlated images. IEEE Conference on Computer Vision and Pattern Recognition (CVPR). 2010:763–770.
42. Candès EJ, Li X, Ma Y, Wright J. Robust principal component analysis? J ACM. 2011; 58(3):11:1–11:37.
43. Chandrasekaran V, Sanghavi S, Parrilo PA, Willsky AS. Rank-sparsity incoherence for matrix decomposition. SIAM Journal on Optimization. 2011; 21(2):572–596.
44. Guo H, Qiu C, Vaswani N. An online algorithm for separating sparse and low-dimensional signal sequences from their sum. IEEE Transactions on Signal Processing. 2014; 62(16):4284–4297.
45. Otazo R, Candès E, Sodickson DK. Low-rank plus sparse matrix decomposition for accelerated dynamic MRI with separation of background and dynamic components. Magnetic Resonance in Medicine. 2015; 73(3):1125–1136. [PubMed: 24760724]

46. Trémoulhéac B, Dikaios N, Atkinson D, Arridge SR. Dynamic mr image reconstruction - separation from undersampled (k,t)-space via low-rank plus sparse prior. IEEE Transactions on Medical Imaging. 2014; 33(8):1689–1701. [PubMed: 24802294]
47. Lingala SG, Hu Y, DiBella E, Jacob M. Accelerated dynamic MRI exploiting sparsity and low-rank structure: k-t SLR. IEEE Transactions on Medical Imaging. 2011; 30(5):1042–1054. [PubMed: 21292593]
48. Zhao B, Haldar JP, Christodoulou AG, Liang ZP. Image reconstruction from highly undersampled (k, t) -space data with joint partial separability and sparsity constraints. IEEE Transactions on Medical Imaging. 2012; 31(9):1809–1820. [PubMed: 22695345]
49. Majumdar A, Ward R. Learning space-time dictionaries for blind compressed sensing dynamic MRI reconstruction. 2015 IEEE International Conference on Image Processing (ICIP). 2015:4550–4554.
50. Pruessmann KP, Weiger M, Börnert P, Boesiger P. Advances in sensitivity encoding with arbitrary k-space trajectories. Magnetic Resonance in Medicine. 2001; 46(4):638–651. [PubMed: 11590639]
51. Majumdar A, Ward RK. Learning the sparsity basis in low-rank plus sparse model for dynamic MRI reconstruction. IEEE International Conference on Acoustics, Speech and Signal Processing (ICASSP). 2015:778–782.
52. Nadakuditi RR. OptShrink: An algorithm for improved low-rank signal matrix denoising by optimal, data-driven singular value shrinkage. IEEE Transactions of Information Theory. 2013; 60(5):3002–3018.
53. Moore BE, Nadakuditi RR, Fessler JA. Dynamic MRI reconstruction using low-rank plus sparse model with optimal rank regularized eigen-shrinkage. Proc ISMRM. May.2014 :740.
54. Moore, BE., Nadakuditi, RR., Fessler, JA. Improved robust PCA using low-rank denoising with optimal singular value shrinkage. 2014 IEEE Workshop on Statistical Signal Processing (SSP); June 2014; p. 13-16.
55. Ravishankar S, Moore BE, Nadakuditi RR, Fessler JA. LASSI: A low-rank and adaptive sparse signal model for highly accelerated dynamic imaging. IEEE Image Video and Multidimensional Signal Processing (IVMSP) workshop. 2016
56. Ravishankar, S., Nadakuditi, RR., Fessler, JA. Efficient sum of outer products dictionary learning (SOUP-DIL) and its application to inverse problems. 2016. preprint: https://www.dropbox.com/s/cog6y48fangkg07/SOUPDIL.pdf?dl=0
57. Gribonval R, Schnass K. Dictionary identification–sparse matrix-factorization via l_1 -minimization. IEEE Trans Inform Theory. 2010; 56(7):3523–3539.
58. Pati Y, Rezaiifar R, Krishnaprasad P. Orthogonal matching pursuit : recursive function approximation with applications to wavelet decomposition. Asilomar Conf on Signals, Systems and Comput. 1993; 1:40–44.
59. Cai JF, Candès EJ, Shen Z. A singular value thresholding algorithm for matrix completion. SIAM Journal on Optimization. 2010; 20(4):1956–1982.
60. Combettes PL, Wajs VR. Signal recovery by proximal forward-backward splitting. Multiscale Modeling & Simulation. 2005; 4(4):1168–1200.
61. Otazo, R. [Online; accessed Mar. 2016] L+S reconstruction Matlab code. 2014. http://cai2r.net/resources/software/ls-reconstruction-matlab-code
62. Woodworth J, Chartrand R. Compressed sensing recovery via nonconvex shrinkage penalties. Inverse Problems. 2016; 32(7):75 004–75 028.
63. Parikh N, Boyd S. Proximal algorithms. Found Trends Optim. Jan; 2014 1(3):127–239.
64. Rockafellar, RT., Wets, RJ-B. Variational Analysis. Heidelberg, Germany: Springer-Verlag; 1998.
65. Sharif B, Bresler Y. Adaptive real-time cardiac MRI using paradise: Validation by the physiologically improved NCAT phantom. IEEE International Symposium on Biomedical Imaging: From Nano to Macro. 2007:1020–1023.
66. Lingala, SG., Hu, Y., DiBella, E., Jacob, M. [Online; accessed 2016] k-t SLR Matlab package. 2014. http://user.engineering.uiowa.edu/~jcb/software/ktslr_matlab/Software.html

Inputs : measurements d, weights λ_L, λ_S, and λ_Z, rank r, upper bound a, number of dictionary learning iterations J, number of proximal gradient iterations $\tilde{J}$, and number of outer iterations $\hat{J}$.

Outputs : reconstructed dynamic image sequence components $x_L^{\hat{J}}$ and $x_S^{\hat{J}}$, learned dictionary $D^{\hat{J}}$, and learned coefficients of patches $Z^{\hat{J}}$.

Initial Estimates: $\left(x_L^0, x_S^0, D^0, Z^0\right)$, with $C^0 = \left(Z^0\right)^H$.

For $t = 1 : \hat{J}$ **repeat**

1) Form $P^{t-1} = \left[P_1 x_S^{t-1} \mid P_2 x_S^{t-1} \mid ... \mid P_M x_S^{t-1}\right]$.
2) **Dictionary Learning:** With training data P^{t-1} and initialization $\left(D^{t-1}, C^{t-1}\right)$, update (c_i, d_i) sequentially for $1 \leq i \leq K$ using (4) (or (8)) and (6). Set (D^t, C^t) to be the output after J cycles of such updates, and $Z^t = (C^t)^H$.
3) **Image Reconstruction:** Update x_L^t and x_S^t using $\tilde{J}$ iterations of the proximal gradient scheme using (9) and (10), and with initialization $\left(x_L^{t-1}, x_S^{t-1}\right)$.

End

Fig. 1.

The LASSI reconstruction algorithms for Problems (P1) and (P2), respectively. Superscript t denotes the iterates in the algorithm. We do not compute the matrices $E_i \triangleq P - \sum_{k \neq i} d_k c_k^H$ explicitly in the dictionary learning iterations. Rather, we efficiently compute products of E_i or E_i^H with vectors [56]. Parameter a is set very large in practice (e.g., $a \propto \| A^\dagger d \|_2$).

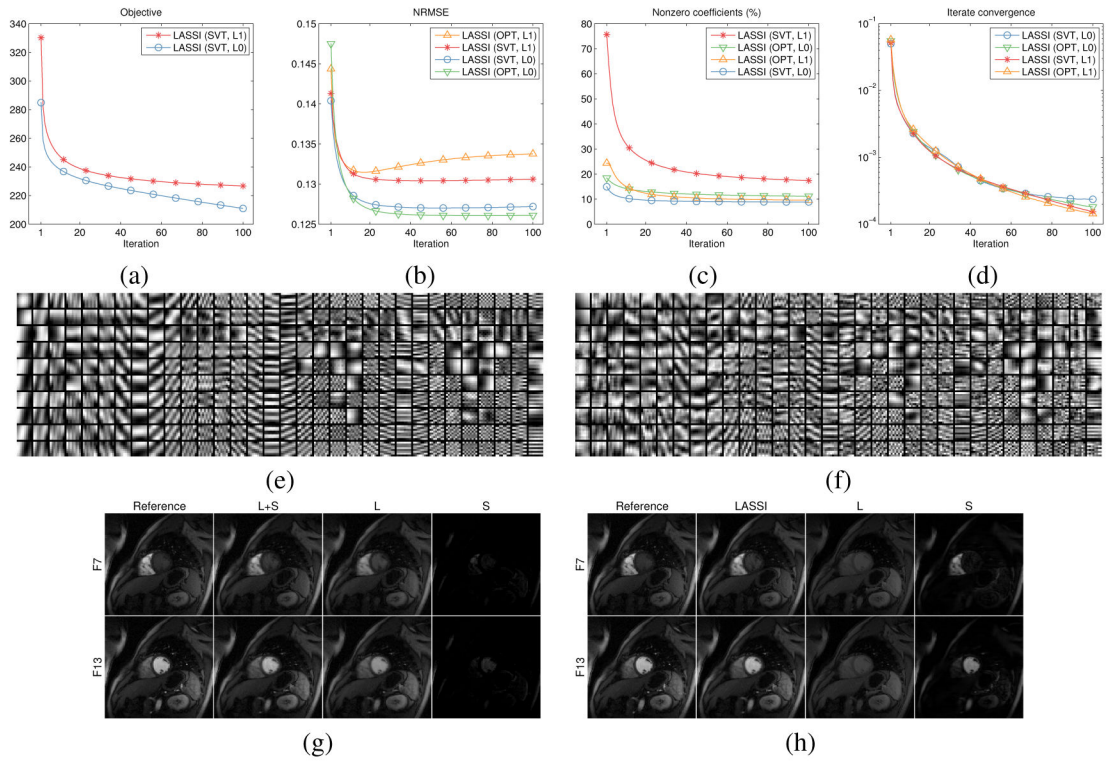

Fig. 2.

Behavior of the LASSI algorithms with Cartesian sampling and 8x undersampling. The algorithms are labeled according to the method used for x_L update, i.e., SVT or OptShrink (OPT), and according to the type of sparsity penalty employed for the patch coefficients (ℓ_0 or ℓ_1 corresponding to (P1) or (P2)). (a) Objectives (shown only for the algorithms for (P1) and (P2) with SVT-based updates, since OPT-based updates do not correspond to minimizing a formal cost function); (b) NRMSE; (c) Sparsity fraction of Z (i.e., $\|Z\|_0/mM$) expressed as a percentage; (d) normalized changes between successive dMRI reconstructions $\|x_L^t + x_S^t - x_L^{t-1} - x_S^{t-1}\|_2 / \|x_{\text{ref}}\|_2$; (e) real and (f) imaginary parts of the atoms of the learned dictionaries in LASSI (using ℓ_0 sparsity penalty and OptShrink-based x_L update) shown as patches – only the 8 × 8 patches corresponding to the first time-point (column) of the rank-1 reshaped (64 × 5) atoms are shown; and frames 7 and 13 of the (g) conventional L+S reconstruction [45] and (h) the proposed LASSI (with ℓ_0 penalty and OptShrink-based x_L update) reconstruction shown along with the corresponding reference frames. The low-rank (L) and (transform or dictionary) sparse (S) components of each reconstructed frame are also individually shown. Only image magnitudes are displayed in (g) and (h).

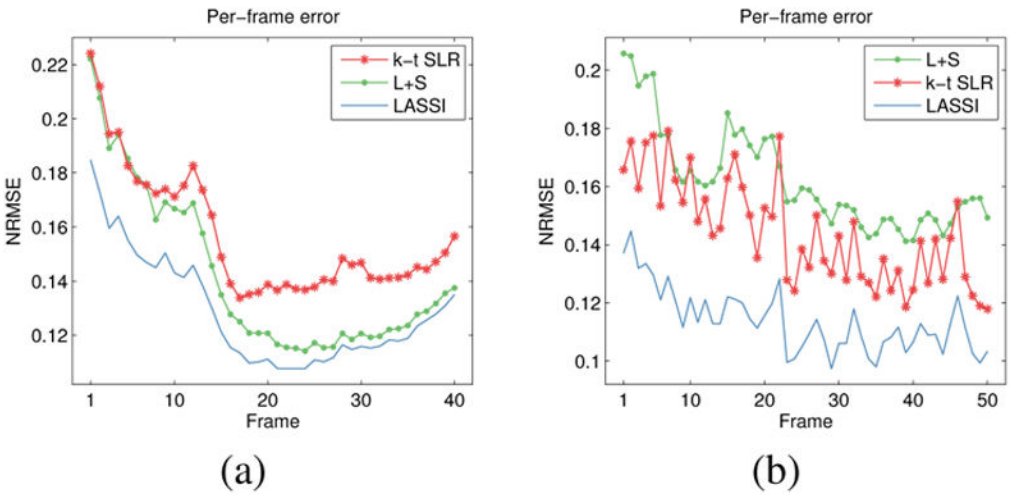

Fig. 3.

NRMSE values computed between each reconstructed and reference frame for LASSI, L+S, and k-t SLR for (a) the cardiac perfusion data [45], [61] at 8x undersampling, and (b) the PINCAT data at 9x undersampling.

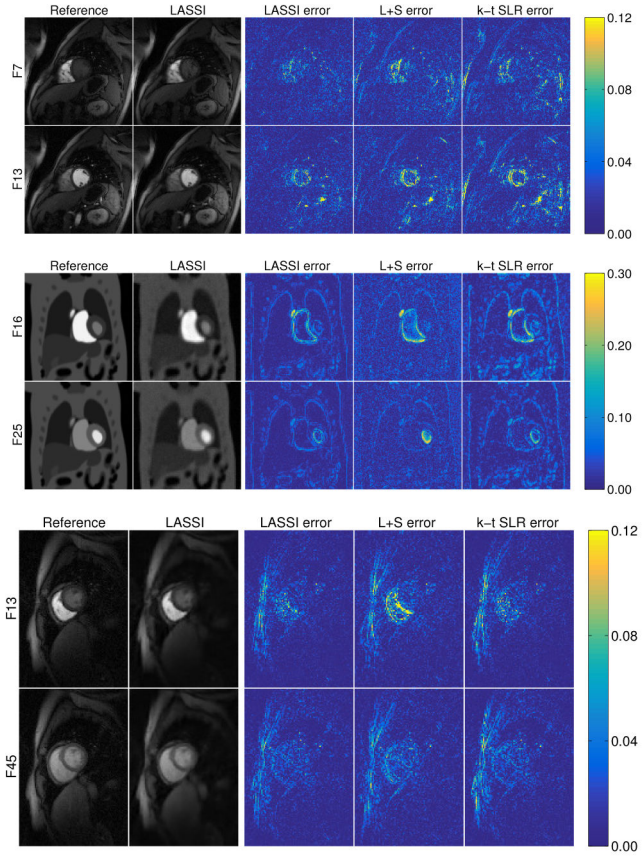

Fig. 4.

LASSI reconstructions and the error maps (clipped for viewing) for LASSI, L+S, and k-t SLR for frames of the cardiac perfusion data [45], [61] (first row), PINCAT data [47], [66] (second row), and *in vivo* myocardial perfusion data [47], [66] (third row), shown along with the reference reconstruction frames. Undersampling factors (top to bottom): 8x, 9x, and 8x. The frame numbers and method names are indicated on the images.

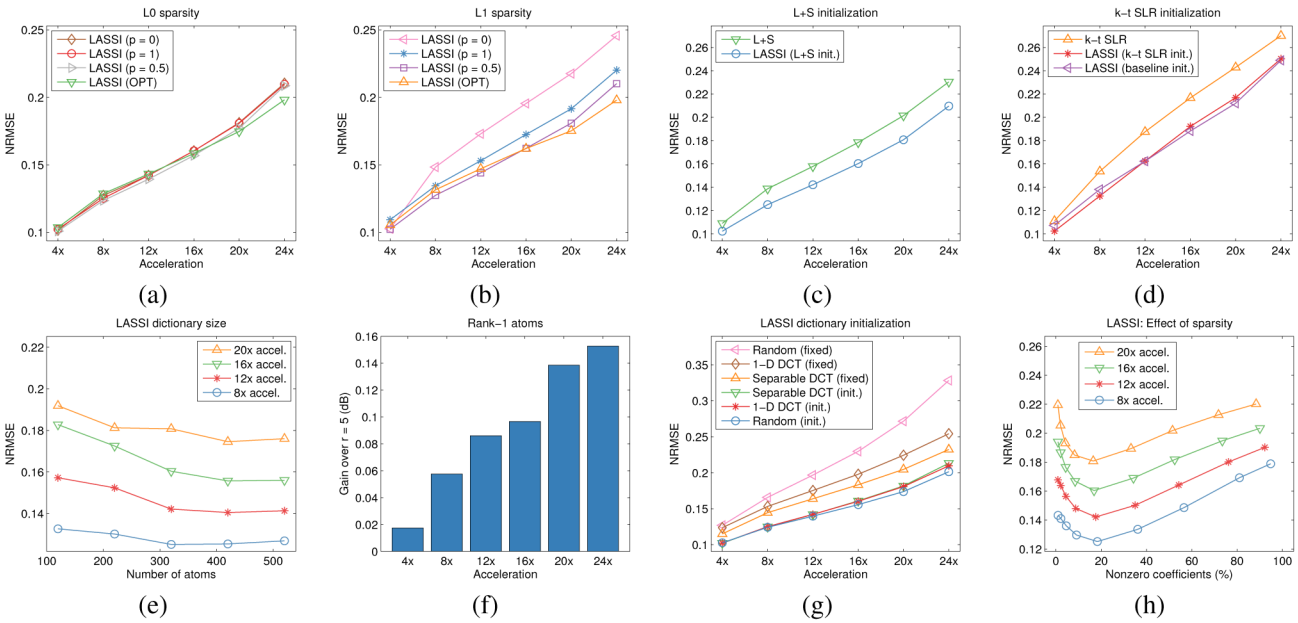

Fig. 5.

Study of LASSI models, methods, and initializations at various undersampling (acceleration) factors for the cardiac perfusion data in [45], [61] with Cartesian sampling: (a) NRMSE for LASSI with ℓ_0 "norm" for sparsity and with x_L updates based on SVT ($p = 1$), OptShrink (OPT), or based on the Schatten p-norm ($p = 0.5$) or rank penalty ($p = 0$); (b) NRMSE for LASSI with ℓ_1 sparsity and with x_L updates based on SVT ($p = 1$), OptShrink (OPT), or based on the Schatten p-norm ($p = 0.5$) or rank penalty ($p = 0$); (c) NRMSE for LASSI when initialized with the output of the L+S method [45] (used to initialize x_S with $x_L^0 = 0$) together with the NRMSE for the L+S method; (d) NRMSE for LASSI when initialized with the output of the k-t SLR method [47] or with the baseline reconstruction (performing zeroth order interpolation at the nonsampled k-t space locations and then backpropagating to image space) mentioned in Section IV-A (these are used to initialize x_S with $x_L^0 = 0$), together with the NRMSE values for k-t SLR; (e) NRMSE versus dictionary size at different acceleration factors; (f) NRMSE improvement (in dB) achieved with $r = 1$ compared to the $r = 5$ case in LASSI; (g) NRMSE for LASSI with different dictionary initializations (a random dictionary, a 320×320 1D DCT and a separable 3D DCT of the same size) together with the NRMSEs achieved in LASSI when the dictionary is fixed to its initial value; and (h) NRMSE versus the fraction of nonzero coefficients (expressed as percentage) in the learned Z at different acceleration factors.

TABLE I

NRMSE values expressed as percentages for the L+S [45], k-t SLR [47], and the proposed DINO-KAT dMRI and LASSI methods at several undersampling (acceleration) factors for the cardiac perfusion data [45], [61] with Cartesian sampling. The NRMSE gain (in decibels (dB)) achieved by LASSI over the other methods is also shown. The best NRMSE for each undersampling factor is in bold.

Undersampling	**4x**	**8x**	**12x**	**16x**	**20x**	**24x**
NRMSE (k-t SLR) %	11.1	15.4	18.8	21.7	24.3	27.0
NRMSE (L+S) %	10.9	13.9	15.8	17.8	20.1	23.0
NRMSE (DINO-KAT) %	10.4	12.6	14.5	16.7	18.8	22.1
NRMSE (LASSI) %	**10.0**	**12.6**	**14.3**	**16.1**	**17.6**	**20.2**
Gain over k-t SLR (dB)	0.9	1.7	2.4	2.6	2.8	2.5
Gain over L+S (dB)	0.7	0.8	0.9	0.9	1.2	1.2
Gain over DINO-KAT (dB)	0.3	0.0	0.1	0.3	0.6	0.8

TABLE II

NRMSE values expressed as percentages for the L+S [45], k-t SLR [47], and the proposed DINO-KAT dMRI and LASSI methods at several undersampling (acceleration) factors for the PINCAT data [47], [66] with pseudo-radial sampling. The best NRMSE values for each undersampling factor are marked in bold.

Undersampling	**5x**	**6x**	**7x**	**9x**	**14x**	**27x**
NRMSE (k-t SLR) %	9.7	10.7	12.2	14.5	18.0	23.7
NRMSE (L+S) %	11.7	12.8	14.2	16.3	19.6	25.4
NRMSE (DINO-KAT) %	8.6	9.5	10.7	12.6	15.9	21.8
NRMSE (LASSI) %	**8.4**	**9.1**	**10.1**	**11.4**	**13.6**	**18.3**
Gain over k-t SLR (dB)	1.2	1.4	1.7	2.1	2.4	2.2
Gain over L+S (dB)	2.8	2.9	3.0	3.1	3.2	2.8
Gain over DINO-KAT (dB)	0.2	0.3	0.6	0.9	1.4	1.5

IEEE Trans Med Imaging. Author manuscript; available in PMC 2017 June 08.

TABLE III

NRMSE values expressed as percentages for the L+S [45], k-t SLR [47], and the proposed DINO-KAT dMRI and LASSI methods at several undersampling (acceleration) factors for the myocardial perfusion MRI data in [47], [66], using pseudo-radial sampling. The best NRMSE values for each undersampling factor are marked in bold.

Undersampling	**4x**	**5x**	**6x**	**8x**	**12x**	**23x**
NRMSE (k-t SLR) %	10.7	11.6	12.7	14.0	16.7	22.1
NRMSE (L+S) %	12.5	13.4	14.6	16.1	18.8	24.2
NRMSE (DINO-KAT) %	10.2	11.0	12.1	13.5	16.4	21.9
NRMSE (LASSI) %	**9.9**	**10.7**	**11.8**	**13.2**	**16.2**	**21.9**
Gain over k-t SLR (dB)	0.7	0.7	0.6	0.5	0.3	0.1
Gain over L+S (dB)	2.1	2.0	1.8	1.7	1.3	0.9
Gain over DINO-KAT (dB)	0.3	0.3	0.2	0.2	0.1	0.0